Duty Cycle Based Model Predictive Control With Hexagonal Virtual Voltage Vectors for Grid-Tied Generation System With the Six-Switch Converter

Paulo Roberto Ubaldo Guazzelli, Stefan Thiago Cury Alves dos Santos,
José Roberto Boffino de Almeida Monteiro, *Member, IEEE*, and Manoel Luís de Aguiar

***Abstract*—The application of duty cycle-based finite control set model predictive control (FCS-MPC) to the six-switch converter (SSC), a reduced switch count multiport converter, faces the drawback of an asymmetrical and limited set of voltage vectors, which deteriorates the quality of the system currents. To overcome this issue, this article proposes an FCS-MPC technique with duty cycle optimization for a wind energy system comprised of SSC, induction generator, and grid connection, for variable speed applications. The main contribution of the technique is the use of a hexagonal set of virtual voltage vectors. Analysis of the experimental results verifies how the proposed technique reduced the grid current THD by over 60% when compared to the equivalent duty cycle-based FCS-MPC without the hexagonal voltage vectors. Additionally, the machine torque ripple factor and the grid active power ripple factors were also reduced. As a result, the proposed control technique boosts the application of the SSC in renewable household wind energy systems.**

***Index Terms*—Finite control set model predictive control (FCS-MPC), reduced switch count converters, six-switch converter (SSC), squirrel cage induction generator, virtual voltage vectors.**

I. INTRODUCTION

GIVEN its inherent synergy to power converters, finite control set model predictive control (FCS-MPC) has been applied to a variety of power converters, such as two-level three-phase inverters [1], [2], [3]; dc/dc converters [4], [5]; HVDC systems [6]; back-to-back 12 switch converters [7], [8]; and multilevel converters [9]. FCS-MPC is based on a finite enumeration of the existing control actions the system can apply at a given instant, and power converters have a finite number of switching combinations since they are made of electronic switches, which can be only turned ON or turned OFF [10]. The choice of the control action is then guided by a designed cost function [11]. Fast dynamics, as well as the simplicity of implementation of not only system restrictions, but also of nonlinearities are among FCS-MPC advantages [12].

Another reason which stimulated the application of FCS-MPC to electrical drives is the availability of consolidated mathematical models in that field, which allows great accuracy in the FCS-MPC required prediction [13]. Predictive torque control (PTC) and predictive current control (PCC) became standards for FCS-MPC control of electrical machinery. PTC requires the adjustment of a weighting factor and provides a lower torque ripple, but also a higher current ripple than PCC. On the other hand, PCC has a higher computational cost, a lower current ripple, and a higher torque ripple than PTC, and yet does not present weighting factors [14]. The grid connection in grid-tied converters has PCC and predictive power control (PPC) as main options [15].

The main concerns in FCS-MPC research have been stability and robustness analysis, new techniques for weighting factors tuning, the prediction with a longer number of horizons, reduction of its computational burden, and its steady-state performance improvement [16], [17], [18]. This article focuses on the latter research topic.

Conventional FCS-MPC applies one voltage vector per cycle of control. This feature is known as the reason for its high ripples in steady-state, and therefore a suboptimal performance [19], [20]. A powerful tool in that regard is the incorporation of a voltage modulator, in a way that FCS-MPC must not only calculate the optimal voltage vector, but also its dwell time at each time step [21]. This new structure brings better steady-state performance, a constant switching frequency, and slower dynamics. Duty cycle based FCS-MPC has been proposed for the two-level voltage converter, as well as for multilevel voltage converters, in different combinations of voltage vectors [22], [23], [24], [25], [26]. Another improvement found on literature is the use of virtual voltage vectors. The original voltage vectors of the converter are arbitrarily combined into a new set for FCS-MPC evaluation. This has been the case for multiphase machine drives, such as a the five-phase permanent magnet

Manuscript received 10 February 2023; revised 26 April 2023 and 11 July 2023; accepted 19 July 2023. Date of publication 26 July 2023; date of current version 1 September 2023. This work was supported in part by Pró-Reitoria de Pesquisa da USP, in part by Conselho Nacional de Desenvolvimento Científico e Tecnológico (CNPq), in part by Coordenação de Aperfeiçoamento de Pessoal de Nível Superior (CAPES) - Finance Code 001, and in part by Fundação de Amparo à Pesquisa do Estado de São Paulo (FAPESP) under Grant 2015/25146-3. Recommended for publication by Associate Editor M. Chen. *(Corresponding author: Paulo Roberto Ubaldo Guazzelli.)*

Paulo Roberto Ubaldo Guazzelli was with the School of Engineering of São Carlos, University of São Paulo, São Carlos 13566-590, Brazil. He is now with the Department of Electrical Engineering, Federal University of São Carlos, São Carlos 13565-905, Brazil (e-mail: paulo.ubaldo@ufscar.br).

Stefan Thiago Cury Alves dos Santos, José Roberto Boffino de Almeida Monteiro, and Manoel Luís de Aguiar are with the School of Engineering of São Carlos, University of São Paulo, São Carlos 13566-590, Brazil (e-mail: stefan.santos@usp.br; jrm@sc.usp.br; aguiar@sc.usp.br).

Color versions of one or more figures in this article are available at https://doi.org/10.1109/TPEL.2023.3299195.

Digital Object Identifier 10.1109/TPEL.2023.3299195

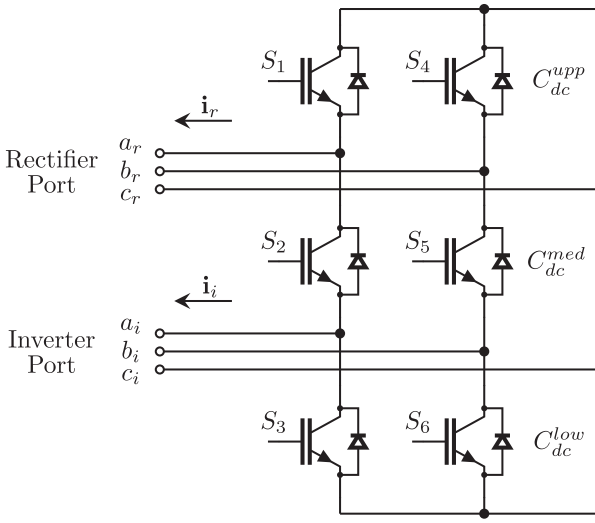

Fig. 1. Six-switch converter (SSC).

motor drive [27], for reduced switch count converters such as the B4 converter [28], and multilevel inverter applications, such as five-level and seven-level converters [29], [30].

Power converter topologies are also a matter of study. Power converters with a reduced number of switches are proposed for systems with aim of size and cost reduction [31]. The six-switch converter (SSC) is a topology that can replace the back-to-back converter in applications that require two independent three-phase ports, but employing only half of its switches [32]. The switch-count reduction comes at the expense of a higher dc bus voltage [33].

The use of SSC becomes attractive in low power scale applications, in which the reduced switch count enables size, weight, and cost reductions [33]. SSC has been applied to uninterrupted power supply (UPS) systems and also applied for wind generation systems with a fully rated converter [34], [35], [36]. Applications also include the SSC as a system with two ac outputs, to power two electrical machines independently from a single dc bus [37], which enables SSC application to electric traction [38]. Additionally, SSC has been applied as a postfault reconfiguration of the nine-switch converter [39]. Fig. 1 shows the SSC circuit, where it can be seen two ac ports, and one dc bus, which doubles as the third leg of the SSC.

Classical control is commonly used for SSC control [33], [34], [35], [36], with PI control loops for each port control, and a PWM signal generation for the switches based on a common carrier signal [33].

FCS-MPC applications in reduced switch count converters include the B4 converter [40], the dual output nine-switch converter [41], and multilevel converters [42]. However, both the use of FCS-MPC and the use of virtual voltage vectors in SSC control have been little exploited in the literature. The discrete behavior of the microprocessors and the limited set of control actions a power converter can provide make FCS-MPC an appealing tool for their control [43]. The authors in [44] applied conventional FCS-MPC in a generation system with the SSC, in two manners: concentrating the two controls (generator and grid) into a single cost function and in a decoupled manner, with separated cost functions. The latter technique provided a better steady-state performance of squirrel cage induction generator (SCIG) torque and dc bus voltage. The authors in [45] incorporated duty cycle optimization into the decoupled FCS-MPC for a grid-tied generation system with the SSC. However, they used an asymmetrical set of voltage vectors, based on the SSC switching combinations. An asymmetrical set of voltage vectors, i.e., a set of voltage vectors with different amplitudes, may lead to output distortions or suboptimal usage of the duty cycle range. Results showed how the performed duty cycle optimization lowered the ripple factors of the SCIG torque and the active power injected onto the grid, however at the cost of a higher grid current total harmonic distortion (THD), due to a current distortion. THD is an important matter in grid-tied systems, being able to quantify the number of harmonics injected onto the grid, and it must be maintained below limits provided by regulations [46].

This work seeks to improve the grid current quality in the duty cycle-based FCS-MPC control for the SSC, fulfilling the gap found in [45]. This article focuses on the use of a new hexagonal set of virtual voltage vectors for the FCS-MPC applied to the SSC. This symmetrical set is responsible for ensuring sinusoidal current outputs. This work proposes a new duty cycle-based decoupled PCC for an SSC grid-tied system. A SCIG is employed as the electrical machine, for power generation. The developed PCC for each subsystem is independent of the other one. A PCC is responsible for the SCIG control in the rectifier port, and another PCC deals with the dc voltage control and power injection onto the grid, through the inverter port. The SCIG torque ripple and the grid active power ripple are the analytical variables that guide the duty cycle optimization. The enumeration of voltage vectors follows a proposed hexagonal set of virtual ones, which allows a better steady-state performance of the system. This work main contributions are as follows:

1) incorporation of a hexagonal set of virtual voltage vectors in duty cycle-based FCS-MPC of an SSC grid-tied generation system;
2) improvement of the FCS-MPC steady-state, mainly the grid current THD, but also the SCIG torque ripple factor, and the grid active power ripple factor, for the SSC.

The rest of this article is organized as follows. After the contribution summarized in Section I, system fundamentals are presented in Section II, with the implementation of the proposed control technique in Section III, and Section IV features the experimental results. Finally, Section V concludes this article.

II. SYSTEM MODELING

A. Reference Frame Orientation

The overall structure of the grid-tied generation system is depicted in Fig. 2. The upper port of SSC is connected to the SCIG. Therefore, this port is herein called as the rectifier port. The SCIG is driven by an independent primer mover. An L filter is connected to the lower port of the SSC and the electrical grid. Therefore, the lower port is herein called the inverter port, consequently. The proposed control system, herein called duty

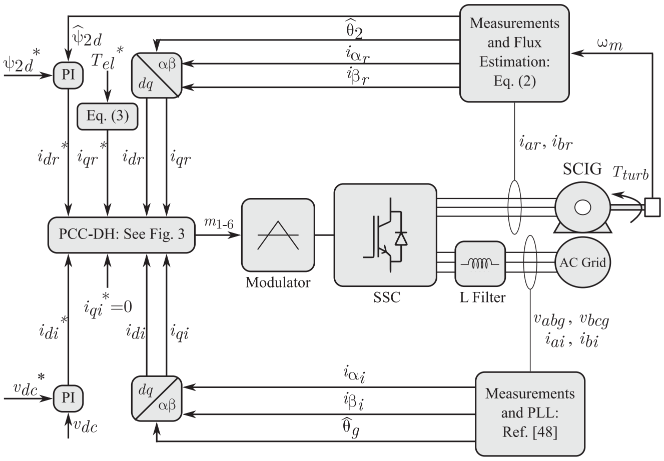

Fig. 2. Macro diagram of the system: grid and SCIG connected to the SSC, with PCC-DH control.

cycle-based PCC with hexagonal-shaped voltage vectors (PCC-DH), sets the modulation indexes m_{1-6} for the six switches, and those values are compared to a triangular carrier.

The SCIG current is labeled as $\mathbf{i}_r$ and is represented in the rotor flux synchronous reference frame of the machine, with direct and quadrature components [47]. Therefore, the current measurements are converted as below

$$\mathbf{i}_r = i_{dr} + j i_{qr} = e^{j\theta_2}\left(i_{\alpha r} + j i_{\beta r}\right) \tag{1}$$

where θ_2 stands for the rotor flux angle and j is the complex operator. This approach allows the rotor flux amplitude to be represented by a scalar value ψ_{2d}. The rotor flux angle and amplitude are estimated as follows:

$$\frac{d\psi_{2d}}{dt} = \frac{R_2 L_H}{L_2} i_{dr} - \frac{R_2}{L_2}\psi_{2d} \tag{2a}$$

$$\omega_2 = p\omega_m + \frac{R_2 L_H}{L_2}\frac{i_{qr}}{\psi_{2d}} \tag{2b}$$

$$\theta_2 = \int \omega_2 dt \tag{2c}$$

where R_2 and L_2 are the SCIG rotor resistance and rotor inductance, respectively; L_H is the SCIG mutual inductance, p is the SCIG number of pole pairs, and ω_2 is the rotor flux angular frequency. The SCIG mechanical speed is given by ω_m. Equation (2b) calculates the rotor flux angular frequency ω_2, which is integrated in (2c) to obtain the rotor flux angle θ_2, used in (1) for the reference frame conversion.

Based on the aforementioned calculation the torque and flux control of the SCIG can be decoupled. Therefore, the direct current reference is given by a PI outer loop which controls the rotor flux amplitude value, and the quadrature current reference i_{qr}^* is given below, based on the desired torque reference T_{el}^* set by the user

$$i_{qr}^* = \frac{1}{K_T}\cdot T_{el}^* = \frac{2L_2}{3pL_H\hat{\psi}_{2d}}\cdot T_{el}^*. \tag{3}$$

Regarding the grid connection, the grid current is labeled as $\mathbf{i}_i$, and is represented in a reference frame which is aligned with the grid voltage amplitude

$$\mathbf{i}_i = i_{di} + j i_{qi} = e^{j\theta_g}\left(i_{\alpha i} + j i_{\beta i}\right) \tag{4}$$

where θ_g is the grid voltage angle, estimated by a phase locked loop (PLL). The synchronous reference frame PLL with moving average filter (MAF-PLL) was employed. Its good performance under unbalanced voltage conditions consolidated its use in three-phase applications [48], [49]. This approach decouples the active and reactive power calculations. Therefore, the direct current i_{di} is proportional to the active power of the inverter port, and its reference i_{di}^* is calculated by a PI outer loop responsible for the dc bus voltage control. The quadrature current i_{qi} is proportional to the injected reactive power, and its reference i_{qi}^* is set to zero.

TABLE I
SSC VOLTAGE VECTORS FOR EACH PORT

[S_1,S_4]	Vector	Amplitude
[1,1]	$\mathbf{v}_1$	$\frac{1}{6}v_{dc}$
[0,1]	$\mathbf{v}_2$	$\frac{\sqrt{13}}{6}v_{dc}$
[0,0]	$\mathbf{v}_3$	$\frac{1}{2}v_{dc}$
[1,0]	$\mathbf{v}_4$	$\frac{\sqrt{13}}{6}v_{dc}$
[S_3,S_6]	**Vector**	**Amplitude**
[1,1]	$\mathbf{v}_5$	$\frac{1}{6}v_{dc}$
[0,1]	$\mathbf{v}_6$	$\frac{\sqrt{13}}{6}v_{dc}$
[0,0]	$\mathbf{v}_7$	$\frac{1}{2}v_{dc}$
[1,0]	$\mathbf{v}_8$	$\frac{\sqrt{13}}{6}v_{dc}$

B. Six-Switch Converter

The SSC has nine possible switching combinations. However, an individual analysis of each port leads to a reduced set of voltage vectors. The voltage at the rectifier port is dependent only on the switching states of the upper switches $[S_1, S_4]$. On the other hand, the switching states of $[S_3, S_6]$ are sufficient to determine the voltage at the inverter port. Therefore, each port has a set of only four voltage vectors, listed in Table I. If $S_l = 1$, the switch is turned ON. If $S_l = 0$, the switch is turned OFF. It can be seen how their amplitudes are asymmetrical.

III. MODEL PREDICTIVE CONTROL

A. PCC-DH

PCC-DH follows the flowchart represented in Fig. 3. Two control structures are executed alternatively. SCIG is executed only in even time steps, and the grid control is executed only in the odd ones. This structure allows the cost functions for each PCC to be calculated separately, instead of merging the control objectives into a single cost function. This approach would lead to one system influencing each other, with FCS-MPC favoring the system variables with the largest values [50]. Decoupled control also does not require the typical delay compensation

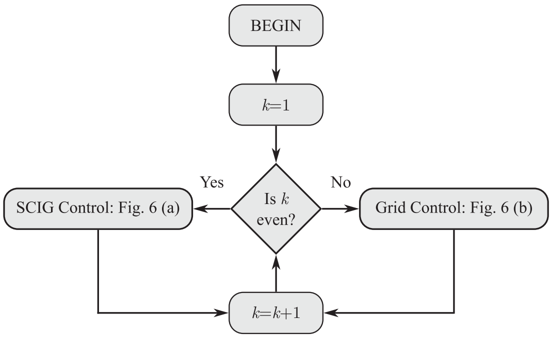

Fig. 3. Control flowchart: PCC-DH.

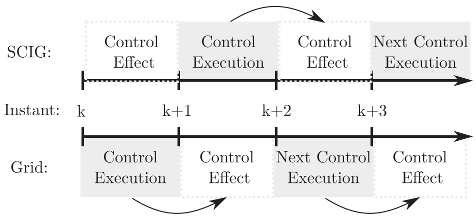

Fig. 4. Time step flow for PCC-DH.

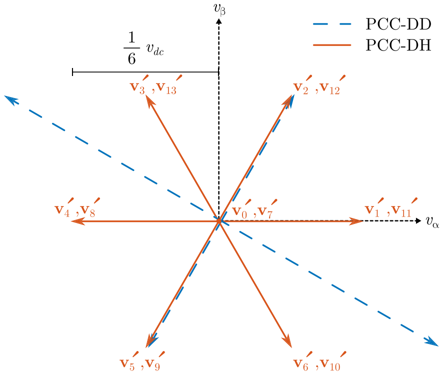

Fig. 5. Hexagonal virtual voltage vectors proposed for the SSC control, next to the existing asymmetrical set of voltage vectors.

calculation of FCS-MPC, since its structure already compensates the delay, due to the presence of a time step gap between two control action calculations, giving time for the control action to properly actuate on the system. For instance, when the SCIG control is executed again, a time step has already passed, in which the system variables suffered the effect from the previous SCIG control execution [50]. Fig. 4 depicts this behavior.

In the decoupled approach, the SCIG and grid control are executed in an alternate manner, in every other step. Based on Table I, only the switching states of S_1 and S_4 will be determined by the SCIG control, and S_3 and S_6 will be turned ON. In the next time step, only the grid control will be performed, and it will calculate the switching states of only S_3 and S_6, while S_1 and S_4 are turned ON.

There are two noteworthy remarks to be made: 1) the control discretization time t_D for each PCC must be twice the sampling time; and 2) the voltage vectors considered by each control must be properly calculated. They must account for the average value between the voltage vectors of the even and odd time steps. The direct application of the decoupled approach to SSC four voltage vectors creates the diamond shape seen in Fig. 5, assuming the capacitors voltages follow the 1:2:1 ratio. This technique, herein called duty cycle-based PCC with diamond-shaped voltage vectors (PCC-DD) [45], is an asymmetrical set of voltage vectors, which also lacks a null voltage vector. However, balanced sinusoidal currents correspond to a circular equidistant shape. Therefore, the hexagonal symmetrical set of voltage vectors seen also in Fig. 5 is proposed.

For the upper port, the proposed virtual voltage vectors $\mathbf{v}_0'$ to $\mathbf{v}_6'$ are

$$\mathbf{v}_0' = \frac{3\mathbf{v}_1 + \mathbf{v}_3}{4} \tag{5a}$$

$$\mathbf{v}_1' = \frac{3\mathbf{v}_1 + \mathbf{v}_4}{4} \tag{5b}$$

$$\mathbf{v}_2' = \mathbf{v}_1 \tag{5c}$$

$$\mathbf{v}_3' = \frac{3\mathbf{v}_1 + \mathbf{v}_2}{4} \tag{5d}$$

$$\mathbf{v}_4' = \frac{2\mathbf{v}_1 + \mathbf{v}_2 + \mathbf{v}_3}{4} \tag{5e}$$

$$\mathbf{v}_5' = \frac{\mathbf{v}_1 + \mathbf{v}_3}{2} \tag{5f}$$

$$\mathbf{v}_6' = \frac{2\mathbf{v}_1 + \mathbf{v}_3 + \mathbf{v}_4}{4}. \tag{5g}$$

As a result, the voltage vectors are calculated according Table I, shown in Appendix A, which also shows the respective modulation indexes M for $[S_1, S_4]$. To achieve the same hexagonal shape, the proposed voltage vectors $\mathbf{v}_7'$ to $\mathbf{v}_{13}'$ for the inverter port are

$$\mathbf{v}_7' = \frac{3\mathbf{v}_5 + \mathbf{v}_7}{4} \tag{6a}$$

$$\mathbf{v}_8' = \frac{3\mathbf{v}_5 + \mathbf{v}_8}{4} \tag{6b}$$

$$\mathbf{v}_9' = \mathbf{v}_5 \tag{6c}$$

$$\mathbf{v}_{10}' = \frac{3\mathbf{v}_5 + \mathbf{v}_6}{4} \tag{6d}$$

$$\mathbf{v}_{11}' = \frac{2\mathbf{v}_5 + \mathbf{v}_6 + \mathbf{v}_7}{4} \tag{6e}$$

$$\mathbf{v}_{12}' = \frac{\mathbf{v}_5 + \mathbf{v}_7}{2} \tag{6f}$$

$$\mathbf{v}_{13}' = \frac{2\mathbf{v}_5 + \mathbf{v}_7 + \mathbf{v}_8}{4}. \tag{6g}$$

Their calculations and the respective modulation indexes M for $[S_3, S_6]$ are also listed in Table I, from Appendix A.

PCC-DH must assign a respective optimal duty cycle δ^{opt} for the optimal voltage vector. As a result, the modulation index m for a given switch is calculated as

$$m_l = \frac{1}{2} + \delta^{opt} M_l - \frac{\delta^{opt}}{2} \tag{7}$$

where $l\,\varepsilon\{1,4\}$ for the SCIG control, and $l\,\varepsilon\{3,6\}$ for the grid control. If $\delta^{opt} = 1$, then $m_l = M_l$ and the chosen virtual voltage vector will be fully applied to the port. If $\delta^{opt} = 0$, the modulation index will be $m_l = 0.5$, and a null voltage vector will be applied to the port.

B. SCIG Control

Fig. 6(a) depicts the overall flowchart for the SCIG control. An iterative loop executes the FCS-MPC characteristic steps of prediction and cost function calculation for each one of the six active voltage vectors set by PCC-DH, as well as the corresponding duty cycle optimization. The voltage vector with the lowest cost is chosen after the finite set is exhaustively evaluated. Then, the control flows into the calculation of the modulation indexes for the lower switches S_3 and S_6, while the

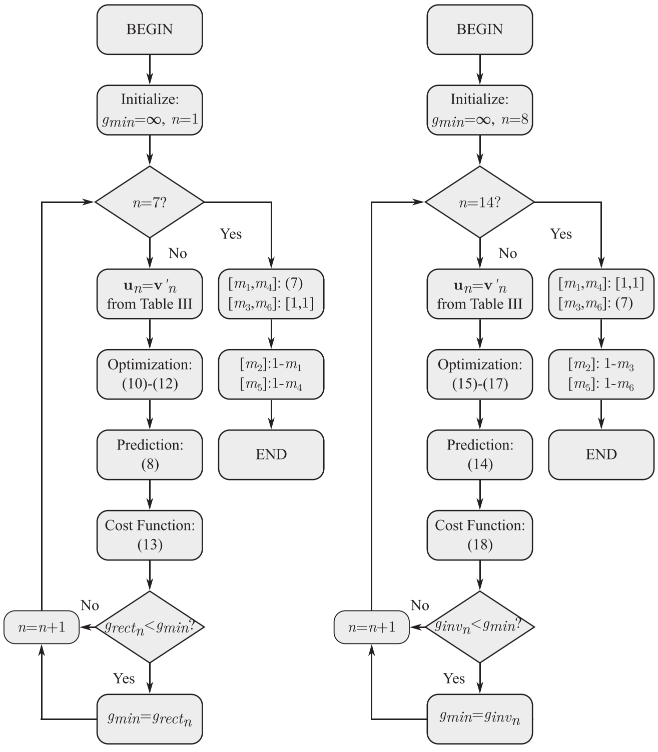

(a) (b)

Fig. 6. Control flowcharts of PCC-DH: SCIG (a) and grid (b) controls. (a) SCIG control. (b) Grid control.

switches S_2 and S_5 are set complementary to them. The upper switches S_1 and S_4 are turned ON.

The prediction of the SCIG dq currents is shown below

$$\mathbf{i}_r^{k+1} = \mathbf{i}_r^k + t_D \left(\frac{L_H}{\sigma L_1 L_2} \left(\frac{R_2}{L_2} - jp\omega_m^k \right) \hat{\psi}_{2d}^k + \frac{\delta_r^{opt} \mathbf{u}_n}{\sigma L_1} + \right.$$
$$\left. - \left(\frac{R_2 L_H^2}{\sigma L_1 L_2^2} + \frac{R_1}{\sigma L_1} + j\omega_2^k \right) \mathbf{i}_r^k \right) \tag{8}$$

where R_1 and L_1 are the SCIG stator resistance and stator inductance, and $\sigma := 1 - \frac{L_H^2}{L_1 L_2}$. Optimal duty cycle δ_r^{opt} is proportional to a dwell time t_r^{opt}. The obtainment of both variables is achieved using the deadbeat principle. The desired performance corresponds to the lowest time the predicted quadrature current i_{qr} will reach its reference

$$i_{qr}^{k+1} = i_{qr}^k + \Delta_r^n t_r^{opt} + \Delta_r^0 \left(t_D - t_r^{opt} \right) \mapsto i_{qr}^* \tag{9}$$

where Δ_r^0 is the derivative term due to the application of a null voltage vector, and Δ_r^n is the derivative term of the SCIG model due to the application of the j voltage vector. As a result

$$\delta_r^{opt} = \frac{t_r^{opt}}{t_D} = \frac{i_{qr}^* - i_{qr}^k - \Delta_r^0 t_D}{t_D \left(\Delta_r^n - \Delta_r^0 \right)} \tag{10}$$

where

$$\Delta_r^0 = -\frac{R_1 L_2^2 + R_2 L_H^2}{\sigma L_1 L_2^2} i_{qr} - \omega_2 i_{dr} - \frac{L_H p \omega_m}{\sigma L_1 L_2} \hat{\psi}_{2d} \tag{11}$$

$$\Delta_r^n = \Delta_r^0 + \frac{u_{qn}}{\sigma L_1}. \tag{12}$$

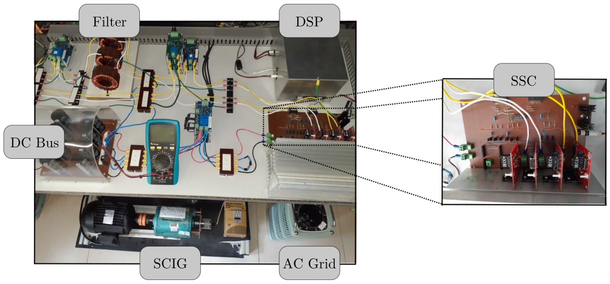

Fig. 7. Laboratory setup for experimental tests.

SCIG control has the cost function shown in (13), based on the quadratic error between the predicted SCIG currents and the SCIG current references

$$g_{rect_n} = \left(i_{dr}^* - \hat{i}_{dr_n}^{k+1} \right)^2 + \left(i_{qr}^* - \hat{i}_{qr_n}^{k+1} \right)^2. \tag{13}$$

C. Grid Control

The overall flowchart for the grid control is illustrated in Fig. 6(b). The PCC iterative loop is executed for the hexagonal set of six virtual voltage vectors, and the one with the lowest cost will determine the modulation indexes of S_3 and S_6, with S_2 and S_5 set complementary to them. On the other hand, S_1 and S_4 will be turned ON.

The calculations in the dq reference frame for current prediction are given by

$$\mathbf{i}_i^{k+1} = \mathbf{i}_i^k + \frac{t_D}{L_f} \left(\delta_i^{opt} \mathbf{u}_n - \mathbf{u}_g^k - R_f \cdot \mathbf{i}_i^k - j\omega_g L_f \mathbf{i}_i^k \right) \tag{14}$$

for a given voltage $\mathbf{u}_n$ applied in the SSC inverter port, with a respective optimal duty cycle δ_i^{opt}. Also, the L filter has inductance L_f and resistance R_f, and t_D is the discretization time, for the forward Euler discretization method.

The dwell time t_r^{opt} calculation follows a similar procedure to the t_i^{opt} calculation. However, optimization is performed on the grid direct current, because this component is proportional to the active power injected into the grid. Therefore, the optimal time t_i^{opt} and the optimal duty cycle δ_i^{opt}, are given by

$$\delta_i^{opt} = \frac{t_i^{opt}}{t_D} = \frac{i_{di}^* - i_{di}^k - \Delta_i^0 t_D}{(\Delta_i^n - \Delta_i^0) t_D} \tag{15}$$

where

$$\Delta_i^0 = \frac{-u_{dg} - R_f i_{di}}{L_f} + \omega_g i_{qi} \tag{16}$$

$$\Delta_i^n = \Delta_i^0 + \frac{u_{dn}}{L_f}. \tag{17}$$

Lastly, the cost function for the grid control follows a similar structure to (13):

$$g_{inv_n} = \left(i_{di}^* - \hat{i}_{di_n}^{k+1} \right)^2 + \left(i_{qi}^* - \hat{i}_{qi_n}^{k+1} \right)^2. \tag{18}$$

IV. RESULTS AND DISCUSSION

Experimental results were obtained in the laboratory setup of Fig. 7. A 73/127 V SCIG and a variable transformer connect to

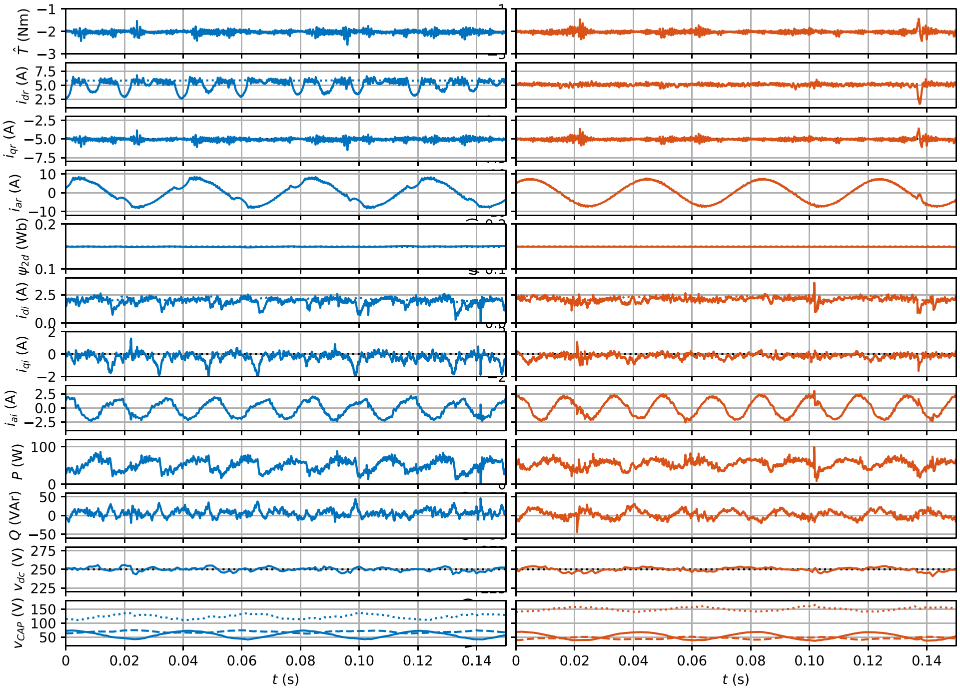

Fig. 8. Experimental results (steady-state at $\omega_m = 800$ rpm and $u_g^{ll} = 20$ V, $T_{el}^* = -2$ Nm, $v_{dc}^* = 250$ V) for PCC-DD (left), and PCC-DH (right)—Top to bottom: SCIG torque, dq currents, phase a current, and rotor flux amplitude; dq grid currents, phase a grid current, active and reactive grid powers, and DC bus voltage, with references in dotted lines. Bottom graph: Upper capacitor (solid), medium capacitor (dotted), and lower capacitor (dashed) voltages.

the SSC, the latter through an L filter. An independent induction motor drives the SCIG at the desired speed, and a floating-point DSP F28379D from Texas Instruments executes the embedded control algorithms. PCC-DD, from [45], whose virtual voltage vectors were also depicted in Fig. 5, was also tested in this setup, for comparison. This technique also employs duty cycle optimization with a modulator. The capacitors were sized according to the C/0.5 C/C ratio of capacitance values from [33]. Table V from Appendix A presents system parameters.

Fig. 8 depicts the experimental results for a steady-state test. It has waveforms of the SCIG speed, torque, dq currents, phase a current, and rotor flux. The torque reference was set to –2 Nm, with the SCIG being driven at the speed of 800 r/min, and a rotor flux of 0.15 Wb, for both techniques.

The –2 Nm torque value corresponds to a quadrature current i_{qr} of 5.5 A. PCC-DD and PCC-DH torque ripple factors of 3.9% and 3.8%, respectively. However, PCC-DD delivered the torque performance at the expense of a low-quality direct current, which lead to a SCIG phase current THD of 13.80%. This distortion was solved by PCC-DH, which decreased the SCIG phase current THD to 3.46%. Harmonic content reduction is beneficial for electric machines since it reduces losses, increases efficiency, and reduces machine thermal and mechanical stress [46], [51].

Additionally, Fig. 8 features the PCC-DD and PCC-DH waveforms for the grid dq currents, phase a current, and grid active and reactive powers for the aforementioned experimental test. The generation system with PCC-DD injected 50 W onto the grid, which corresponded to a direct current i_{di} of 1.90 A. PCC-DH, however, injected 54 W for a direct current i_{di} of 2.08 A. PCC-DH managed to reduce the ripples of both the direct current i_{di} and the quadrature current i_{qi}. As a result, the THD of the grid phase a current decreased from 15.5% to 5.5%, a 64% reduction. The grid current total demand distortion (TDD) was reduced from 1.94% to 0.82%, a 58% reduction. In both cases, the system complies with the TDD limit of 5% set by IEEE [46]. Additionally, the active power ripple factor also decreased, going from 27.9% to 20.8%. Fig. 8 also depicts the dc bus voltage and the voltages for each capacitor in the SSC. PCC-DD had upper, medium, and lower capacitors voltages with mean values of 58, 123, and 68 V, respectively. On the other hand, PCC-DH featured the respective mean values of 53, 150, and 47 V for the upper, medium, and lower capacitors.

TABLE II
SIMULATED AVERAGE SWITCHING FREQUENCIES

SSC switches	PCC-DD	PCC-DH
Top switches (S_1 and S_4)	9.8 kHz	9.9 kHz
Middle switches (S_2 and S_5)	19.2 kHz	19.6 kHz
Bottom switches (S_3 and S_6)	9.4 kHz	9.7 kHz

Simulation results for the same steady-state test were developed in MATLAB/Simulink, with the same conditions from the experimental test. The simulation was made in order to analyze the average switching frequencies of both techniques, since the switching losses of SSC are influenced by the switching frequency [33]. The graphics of Fig. 9 show how both techniques managed to control the power generation system, with the same current quality differences between PCC-DD and PCC-DH seen in the experimental results. Table II depicts the average switching frequencies on the SSC switches, according to the simulations results. The middle switches featured an average switching

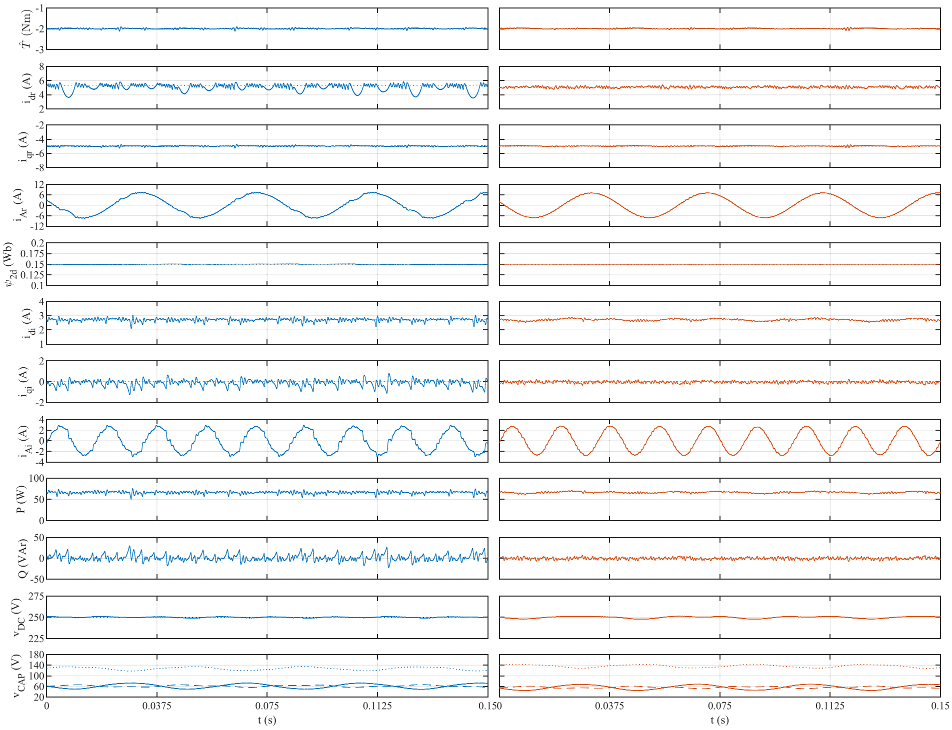

Fig. 9. Simulated results (steady-state at $\omega_m = 800$ r/min and $u_g^{ll} = 20$ V, $T_{el}^* = -2$ Nm, $v_{dc}^* = 250$ V) for PCC-DD (left), and PCC-DH (right)—Top to bottom: SCIG torque, dq currents, phase a current, and rotor flux amplitude; dq grid currents, phase a grid current, active and reactive grid powers, and DC bus voltage, with references in dotted lines. Bottom graph: Upper capacitor (solid), medium capacitor (dotted), and lower capacitor (dashed) voltages.

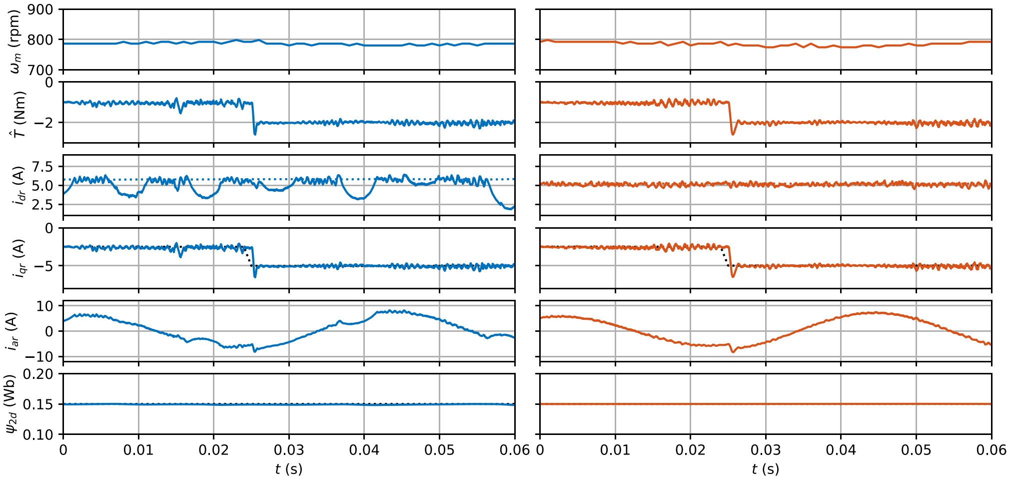

Fig. 10. Experimental results (dynamical test at $\omega_m = 800$ r/min and $u_g^{ll} = 20$ V, with step change at 0.025 s of T_{el}^* from -1 to -2 Nm, $v_{dc}^* = 250$ V) for the PCC-DD (left), and PCC-DH (right)—Top to bottom: SCIG speed, torque, dq currents, phase a current, and rotor flux amplitude, with references in dotted lines.

frequency close to the 20 kHz of the carrier frequency, while the upper and lower switches featured switching frequencies closer to half of this value. This is expected since the middle switches are shared by both the SCIG and the grid ports.

Additionally, PCC-DH provided average switching frequencies no more than 5% higher than the ones of PCC-DD.

The second experimental test of this article is a torque step change, which enables the evaluation of the techniques' dynamic performance. The torque step occurs at 0.025 s in the graphs from Fig. 10, and changes from -1 to –2 Nm, with the SCIG at 800 r/min, for a 0.06 s time window. PCC-DD and PCC-DH both reached the new torque reference, showing no interference on the flux-related variables, that is, the rotor flux amplitude and rotor and the i_{dr} direct current. The greater torque reference increased the i_{qr} current value. Both techniques featured very fast dynamics, with a settling time of 0.30 ms for PCC-DD and 0.40 ms for PCC-DH, and an overshoot of 31.0% for PCC-DD and of 30.1% for PCC-DH.

On the other hand, PCC-DH results for the same dynamics test are shown in Fig. 11. The time window of 0.4 s is larger than the

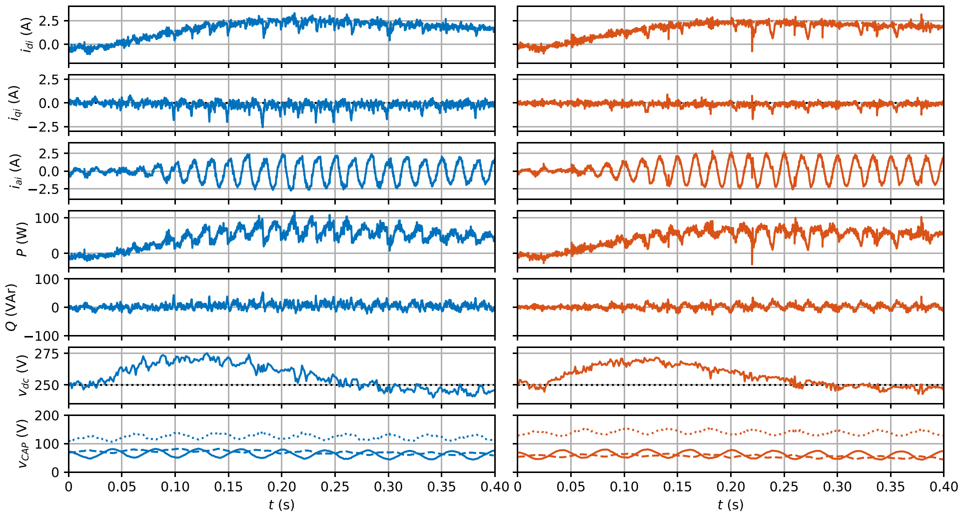

Fig. 11. Experimental results (dynamical test at $\omega_m = 800$ rpm and $u_g^{ll} = 20$ V, with step change at 0.025 s of T_{el}^* from -1 to -2 Nm, $v_{dc}^* = 250$ V) for the PCC-DD (left), and PCC-DH (right)—Top to bottom: dq grid currents, phase a grid current, active and reactive grid powers, and DC bus voltage, with references in dotted lines. Bottom graph: Upper capacitor (solid), medium capacitor (dotted), and lower capacitor (dashed) voltages.

one from Fig. 10 because the grid-related variables have a slower response than the ones from the SCIG. This happens due to the presence of a PI controller in the dc voltage control loop. Both systems were working below the whole power consumption for the –1 Nm torque input. The greater torque reference increased the SCIG power output, causing an overshoot in the dc bus voltage. The control system treated this feature, which increased the i_{di} current reference, and therefore changed the direct current from –0.4 A to 1.7 A for PCC-DD, and from –0.3 A to 1.9 A in the case of PCC-DH. Consequently, the active power injected onto the grid changed from a consumption of 8 W to a generation of 48 W, for PCC-DD, and changed from a consumption of 7 W to a generation of 54 W, for PCC-DH. The i_{qi} quadrature current was controlled at zero during the whole test, and as a result the reactive power injected onto the grid also maintained itself at zero.

Computational burden can be a critical factor for embedded systems. PCC-DD had a burden of 11.3 μs, and PCC-DH increased this value to 13.4 μs. This issue is due to the enumeration of voltage vectors going from 4 to 6 voltage vectors at each PCC execution. As a result, the computational burden increased by 18.6%, with a resulting 64.5% grid current THD reduction, a 2.6% torque ripple factor reduction, a 75% SCIG current THD reduction, and a 25.5% active power ripple factor reduction. Table III summarizes the aforementioned performance indexes for PCC-DD and PCC-DH.

TABLE III
PERFORMANCE INDEXES OF PCC-DD AND PCC-DH

Performance Index	PCC-DD	PCC-DH
Torque ripple factor (%)	3.9	3.8
Active power ripple factor (%)	27.9	20.8
SCIG current THD (%)	13.80	3.46
Grid current THD (%)	15.5	5.5
Grid current TDD (%)	1.94	0.85
Torque settling time (ms)	0.30	0.40
Torque overshoot (%)	31.0	30.1
Computational burden (μs)	11.3	13.4

V. CONCLUSION

SSC usage in household wind energy applications requires attention to high-performance control techniques. FCS-MPC is an interesting candidate for it, due to its advantages, such as fast dynamics, ease of implementation, and inherent synergy with power converters. FCS-MPC use becomes even more appealing with the incorporation of duty cycle optimization theory, which enhances its steady-state performance. However, the voltage vectors from SSC are asymmetrically sized, which means the larger ones have a range of useful duty cycles smaller than the ideal, in order to provide sinusoidal outputs.

The proposed control technique, PCC-DH, overcame this issue by means of a hexagonal set of virtual voltage vectors, equally sized in amplitude. The duty cycle and switching state combinations for each voltage vector were properly mapped, and the PCC for each subsystem was independently developed, in a decoupled manner. SSC upper port connects to the generation unit, a SCIG, and the lower port connects to the grid by means of an L filter. FCS-MPC is responsible for the control of both subsystems, and also for the control of the SSC dc bus voltage.

Experimental results validated PCC-DH, with a sensible improvement on the grid current THD, fulfilling the gap found in the literature, specifically in PCC-DD [45]. Additionally, the original advantages of torque and active power steady-state performances did not deteriorate, but even improved. This steady-state improvement, provided by the hexagonal set of virtual voltage vectors, overcomes the increase in the technique computational burden, deeming the exchange well worth it. Therefore, PCC-DH enhances the desirability of duty cycle-based FCS-MPC application in household wind power generation systems with the SSC.

APPENDIX A

See Tables IV and V.

TABLE IV
AVERAGE VOLTAGE VECTORS CONSIDERED BY PCC-DH

$[M_1,M_4]$	Vector	v_α	v_β
[0.5,0.5]	$\mathbf{v}'_0$	$\frac{3v_{upp}-v_{med}-v_{low}}{12}$	$\frac{\sqrt{3}(3v_{upp}-v_{med}-v_{low})}{12}$
[1,0.5]	$\mathbf{v}'_1$	$\frac{5v_{upp}+v_{med}+v_{low}}{12}$	$\frac{\sqrt{3}(3v_{upp}-v_{med}-v_{low})}{12}$
[1,1]	$\mathbf{v}'_2$	$\frac{v_{upp}}{3}$	$\frac{\sqrt{3}v_{upp}}{3}$
[0.5,1]	$\mathbf{v}'_3$	$\frac{v_{upp}-v_{med}-v_{low}}{6}$	$\frac{\sqrt{3}v_{upp}}{3}$
[0,0.5]	$\mathbf{v}'_4$	$\frac{v_{upp}-3v_{med}-3v_{low}}{12}$	$\frac{\sqrt{3}(3v_{upp}-v_{med}-v_{low})}{12}$
[0,0]	$\mathbf{v}'_5$	$\frac{v_{upp}-v_{med}-v_{low}}{6}$	$\frac{\sqrt{3}(v_{upp}-v_{med}-v_{low})}{6}$
[0.5,0]	$\mathbf{v}'_6$	$\frac{v_{upp}}{3}$	$\frac{\sqrt{3}(v_{upp}-v_{med}-v_{low})}{6}$
$[M_3,M_6]$	Vector	v_α	v_β
[0.5,0.5]	$\mathbf{v}'_7$	$\frac{-3v_{upp}+v_{med}+v_{low}}{12}$	$\frac{\sqrt{3}(-v_{upp}+v_{med}+v_{low})}{12}$
[1,0.5]	$\mathbf{v}'_8$	$\frac{-4v_{upp}-v_{med}-2v_{low}}{12}$	$\frac{\sqrt{3}(-2v_{upp}+v_{med})}{12}$
[1,1]	$\mathbf{v}'_9$	$\frac{-v_{upp}}{3}$	$\frac{-\sqrt{3}v_{upp}}{3}$
[0.5,1]	$\mathbf{v}'_{10}$	$\frac{-v_{upp}+2v_{med}-v_{low}}{12}$	$\frac{\sqrt{3}(-3v_{upp}+v_{low})}{12}$
[0,0.5]	$\mathbf{v}'_{11}$	$\frac{3v_{med}+2v_{low}}{12}$	$\frac{\sqrt{3}(2v_{upp}+v_{med})}{12}$
[0,0]	$\mathbf{v}'_{12}$	$\frac{-v_{upp}+v_{med}+v_{low}}{6}$	$\frac{\sqrt{3}(-v_{upp}+v_{med}+v_{low})}{6}$
[0.5,0]	$\mathbf{v}'_{13}$	$\frac{-3v_{upp}+v_{low}}{12}$	$\frac{\sqrt{3}(-v_{upp}+2v_{med}+v_{low})}{12}$

TABLE V
SYSTEM PARAMETERS

Parameter	Value	Unit
R_s	0.8088	Ω
R_r	0.2648	Ω
L_s and L_r	33.1	mH
L_H	29.5	mH
p	2	—
v_{dc}^*	250	V
C_{dc}^{upp}/C_{dc}^{med}/C_{dc}^{low}	3000/1500/3000	μF
L_f	8.5	mH
R_f	0.167	Ω
Line-to-line grid voltage	20	V
Maximum grid current	10	A
Grid frequency	60	Hz
ψ_{2d} PI proportional gain	40	$\frac{Wb}{V}$
ψ_{2d} PI integral gain	400	$\frac{Wb}{V\cdot s}$
v_{dc} PI proportional gain	0.05	$\frac{A}{V}$
v_{dc} PI integral gain	0.9	$\frac{A}{V\cdot s}$
Preprocessing (low-pass filter)	660	Hz
Measurement frequency	20	kHz
Control frequency	10	kHz

REFERENCES

[1] J. Rodriguez, R. M. Kennel, J. R. Espinoza, M. Trincado, C. A. Silva, and C. A. Rojas, "High-performance control strategies for electrical drives: An experimental assessment," *IEEE Trans. Ind. Electron.*, vol. 59, no. 2, pp. 812–820, Feb. 2012.

[2] H. Xie, F. Wang, Q. Chen, Y. He, J. Rodríguez, and R. Kennel, "Computationally efficient predictive current control with finite set extension using derivative projection for IM drives," *IEEE J. Emerg. Sel. Topics Power Electron.*, vol. 11, no. 2, pp. 1345–1357, 2023.

[3] S. Vazquez, E. Zafra, R. P. Aguilera, T. Geyer, J. I. Leon, and L. G. Franquelo, "Prediction model with harmonic load current components for FCS-MPC of an uninterruptible power supply," *IEEE Trans. Power Electron.*, vol. 37, no. 1, pp. 322–331, Jan. 2022.

[4] C. Restrepo, G. Garcia, F. Flores-Bahamonde, D. Murillo-Yarce, J. I. Guzman, and M. Rivera, "Current control of the coupled-inductor buck–boost DC–DC switching converter using a model predictive control approach," *IEEE J. Emerg. Sel. Topics Power Electron.*, vol. 8, no. 4, pp. 3348–3360, Dec. 2020.

[5] R. Razani and Y. A.-R. I. Mohamed, "Model predictive control of non-isolated DC/DC modular multilevel converter improving the dynamic response," *IEEE Open J. Power Electron.*, vol. 3, pp. 303–316, 2022.

[6] J.-W. Moon, J.-S. Gwon, J.-W. Park, D.-W. Kang, and J.-M. Kim, "Model predictive control with a reduced number of considered states in a modular multilevel converter for HVDC system," *IEEE Trans. Power Del.*, vol. 30, no. 2, pp. 608–617, Apr. 2015.

[7] S. Odhano, S. Rubino, M. Tang, P. Zanchetta, and R. Bojoi, "Stator current-sensorless-modulated model predictive direct power control of a DFIM with magnetizing characteristic identification," *IEEE J. Emerg. Sel. Topics Power Electron.*, vol. 9, no. 3, pp. 2797–2806, Jun. 2021.

[8] A. J. Sguarezi Filho, A. L. de Oliveira, L. L. Rodrigues, E. C. M. Costa, and R. V. Jacomini, "A robust finite control set applied to the DFIG power control," *IEEE J. Emerg. Sel. Topics Power Electron.*, vol. 6, no. 4, pp. 1692–1698, Dec. 2018.

[9] I. Harbi, M. Ahmed, C. M. Hackl, J. Rodriguez, R. Kennel, and M. Abdelrahem, "Low-complexity dual-vector model predictive control for single-phase nine-level ANPC-based converter," *IEEE Trans. Power Electron.*, vol. 38, no. 3, pp. 2956–2971, Mar. 2023.

[10] S. Kouro, M. A. Perez, J. Rodriguez, A. M. Llor, and H. A. Young, "Model predictive control: MPC€s role in the evolution of power electronics," *IEEE Ind. Electron. Mag.*, vol. 9, no. 4, pp. 8–21, Dec. 2015.

[11] S. Kouro, P. Cortes, R. Vargas, U. Ammann, and J. Rodriguez, "Model predictive control–A simple and powerful method to control power converters," *IEEE Trans. Ind. Electron.*, vol. 56, no. 6, pp. 1826–1838, Jun. 2009.

[12] S. Vazquez, J. Rodriguez, M. Rivera, L. G. Franquelo, and M. Norambuena, "Model predictive control for power converters and drives: Advances and trends," *IEEE Trans. Ind. Electron.*, vol. 64, no. 2, pp. 935–947, Feb. 2017.

[13] J. Rodriguez et al., "Latest advances of model predictive control in electrical drives–Part I: Basic concepts and advanced strategies," *IEEE Trans. Power Electron.*, vol. 37, no. 4, pp. 3927–3942, Apr. 2022.

[14] F. Wang, S. Li, X. Mei, W. Xie, J. Rodriguez, and R. M. Kennel, "Model-based predictive direct control strategies for electrical drives: An experimental evaluation of PTC and PCC methods," *IEEE Trans. Ind. Informat.*, vol. 11, no. 3, pp. 671–681, Jun. 2015.

[15] S. S. Lee, Y. E. Heng, and M. A. Roslan, "Finite control set model predictive control of nine-switch AC/DC/AC converter," in *Proc. IEEE Int. Conf. Power Energy*, 2016, pp. 746–751.

[16] M. F. Elmorshedy, W. Xu, F. F. M. El-Sousy, M. R. Islam, and A. A. Ahmed, "Recent achievements in model predictive control techniques for industrial motor: A comprehensive state-of-the-art," *IEEE Access*, vol. 9, pp. 58170–58191, 2021.

[17] P. Karamanakos, E. Liegmann, T. Geyer, and R. Kennel, "Model predictive control of power electronic systems: Methods, results, and challenges," *IEEE Open J. Ind. Appl.*, vol. 1, pp. 95–114, 2020.

[18] F. Wang, X. Mei, J. Rodriguez, and R. Kennel, "Model predictive control for electrical drive systems-an overview," *CES Trans. Electr. Mach. Syst.*, vol. 1, no. 3, pp. 219–230, Sep. 2017.

[19] J. J. Aciego, I. G. Prieto, M. J. Duran, M. Bermudez, and P. Salas-Biedma, "Model predictive control based on dynamic voltage vectors for six-phase induction machines," *IEEE J. Emerg. Sel. Topics Power Electron.*, vol. 9, no. 3, pp. 2710–2722, Jun. 2021.

[20] J. J. Aciego, I. G. Prieto, and M. J. Duran, "Model predictive control of six-phase induction motor drives using two virtual voltage vectors," *IEEE J. Emerg. Sel. Topics Power Electron.*, vol. 7, no. 1, pp. 321–330, Mar. 2019.

[21] Y. Zhang and H. Yang, "Model predictive torque control of induction motor drives with optimal duty cycle control," *IEEE Trans. Power. Electron.*, vol. 29, no. 12, pp. 6593–6603, Dec. 2014.

[22] Z. Song, Y. Tian, W. Chen, Z. Zou, and Z. Chen, "Predictive duty cycle control of three-phase active-front-end rectifiers," *IEEE Trans. Power Electron.*, vol. 31, no. 1, pp. 698–710, Jan. 2016.

[23] X. Zhang, L. Tan, J. Xian, and H. Zhang, "Three vector complete model predictive control for three-phase grid-connected inverters with LCL filter," in *Proc. IEEE 13th Conf. Ind. Electron. Appl.*, 2018, pp. 1470–1475.

[24] Y. Zhang, W. Xie, Z. Li, and Y. Zhang, "Model predictive direct power control of a PWM rectifier with duty cycle optimization," *IEEE Trans. Power Electron.*, vol. 28, no. 11, pp. 5343–5351, Nov. 2013.

[25] J.-H. Lee, J.-S. Lee, H.-C. Moon, and K.-B. Lee, "An improved finite-set model predictive control based on discrete space vector modulation methods for grid-connected three-level voltage source inverter," *IEEE J. Emerg. Sel. Topics Power Electron.*, vol. 6, no. 4, pp. 1744–1760, Dec. 2018.

[26] B. Hu, L. Kang, J. Cheng, X. Luo, and Z. Zhang, "Model predictive power control with dual vectors for three-level inverter," *IEEE J. Emerg. Sel. Topics Power Electron.*, vol. 7, no. 4, pp. 2204–2212, Dec. 2019.

[27] M. S. R. Saeed, W. Song, L. Huang, and B. Yu, "Double-vector-based finite control set model predictive control for five-phase PMSMs with high tracking accuracy and DC-link voltage utilization," *IEEE Trans. Power Electron.*, vol. 37, no. 12, pp. 15234–15244, Dec. 2022.

[28] C.-K. Lin, J.-T. Yu, Y.-S. Lai, H.-C. Yu, and C.-I. Peng, "Two-vector-based modeless predictive current control for four-switch inverter-fed synchronous reluctance motors emulating the six-switch inverter operation," *Electron. Lett.*, vol. 52, no. 14, pp. 1244–1246, 2016.

[29] D. Zhou, L. Ding, and Y. Li, "Two-stage optimization-based model predictive control of 5L-ANPC converter-fed PMSM drives," *IEEE Trans. Ind. Electron.*, vol. 68, no. 5, pp. 3739–3749, May 2021.

[30] Y. Li and Y. Zhao, "A virtual space vector model predictive control for a seven-level hybrid multilevel converter," *IEEE Trans. Power Electron.*, vol. 36, no. 3, pp. 3396–3407, Mar. 2021.

[31] C. B. Jacobina, M. B. de R. Correa, A. M. N. Lima, and E. R. C. da Silva, "AC motor drive systems with a reduced-switch-count converter," *IEEE Trans. Ind. Appl.*, vol. 39, no. 5, pp. 1333–1342, Sep./Oct. 2003.

[32] M. Shibata and N. Hoshi, "Novel inverter topologies for two-wheel drive electric vehicles with two permanent magnet synchronous motors," in *Proc. IEEE Eur. Conf. Power Electron. Appl.*, 2007, pp. 1–10.

[33] M. Heydari, A. Fatemi, and A. Y. Varjani, "A reduced switch count three-phase AC/AC converter with six power switches: Modeling, analysis, and control," *IEEE J. Emerg. Sel. Topics Power Electron.*, vol. 5, no. 4, pp. 1720–1738, Dec. 2017.

[34] M. Heydari, A. Y. Varjani, and M. Mohamadian, "A novel variable-speed wind energy system using induction generator and six-switch AC/AC converter," in *Proc. 3rd Power Electron. Drive Syst. Technol.*, 2012, pp. 244–250.

[35] A. Ajami, R. Alizadeh, and M. Elmi, "Design and control of a grid tied 6-switch converter for two independent low power wind energy resources based on PMSGs with MPPT capability," *Renewable Energy*, vol. 87, pp. 532–543, 2016.

[36] M. Heydari and K. Smedley, "A cost-effective sensorless variable-speed wind energy system," in *Proc. 6th Power Electron., Drive Syst. Technol. Conf.*, 2015, pp. 597–602.

[37] E. S. Najmi, A. H. Rajaei, M. Mohamadian, and S. M. Dehghan, "A novel dual output six switch inverter for driving two phase induction motor," in *Proc. 4th Annu. Int. Power Electron., Drive Syst. Technol. Conf.*, 2013, pp. 248–253.

[38] M. Al Sakka et al., "Comparative analysis of single-input multi-output inverter topologies for multi-motor drive systems," in *Proc. 15th Int. Conf. Ecological Veh. Renewable Energies*, 2020, pp. 1–12.

[39] E. S. Najmi, S. M. Dehghan, M. Heydari, M. Mohamadian, A. Yazdian, and G. S. Milan, "Fault tolerant nine switch inverter," in *Proc. 2nd Power Electron., Drive Syst. Technol. Conf.*, 2011, pp. 534–539.

[40] Z. Li, J. Xia, X. Gao, Y. Guo, and X. Zhang, "Dual-vector-based predictive torque control for fault-tolerant inverter-fed induction motor drives with adaptive switching instant," *IEEE Trans. Ind. Electron.*, vol. 70, no. 12, pp. 12003–12013, Dec. 2023.

[41] O. Gulbudak and M. Gokdag, "Asymmetrical multi-step direct model predictive control of nine-switch inverter for dual-output mode operation," *IEEE Access*, vol. 7, pp. 164720–164733, 2019.

[42] X. Xing, M. Jing, C. Du, C. Qin, C. Liu, and Z. Chen, "An adaptive model predictive control for reduced switch count three-level inverter," *IEEE J. Emerg. Sel. Topics Power Electron.*, vol. 11, no. 1, pp. 453–464, Feb. 2023.

[43] J. Rodriguez et al., "Latest advances of model predictive control in electrical drives–Part II: Applications and benchmarking with classical control methods," *IEEE Trans. Power Electron.*, vol. 37, no. 5, pp. 5047–5061, May 2021.

[44] P. R. U. Guazzelli, A. G. de Castro, S. T. C. A. D. Santos, C. M. R. de Oliveira, J. R. B. A. Monteiro, and M. L. de Aguiar, "Finite control set model based predictive control of grid-tied six-switch converter applied to induction generator," in *Proc. IEEE 15th Braz. Power Electron. Conf. IEEE 5th Southern Power Electron. Conf.*, 2019, pp. 1–6.

[45] P. R. U. Guazzelli, S. T. C. A. D. Santos, J. R. B. de A. Monteiro, and M. L. de Aguiar, "Model predictive control with duty cycle optimization and virtual null vector for induction generator with six switch converter," *IEEE J. Emerg. Sel. Topics Power Electron.*, vol. 11, no. 2, pp. 1422–1431, Apr. 2023.

[46] *IEEE Recommended Practice and Requirements for Harmonic Control in Electric Power Systems - Redline*, IEEE Standard 519-2014 (Revision of IEEE Standard 519-1992), Jun. 2014.

[47] P. Vas, *Vector Control of AC Machines* (Monographs in Electrical and Electronic Engineering Series). Oxford, England: Clarendon Press, 1990.

[48] S. Golestan, M. Ramezani, J. M. Guerrero, F. D. Freijedo, and M. Monfared, "Moving average filter based phase-locked loops: Performance analysis and design guidelines," *IEEE Trans. Power Electron.*, vol. 29, no. 6, pp. 2750–2763, Jun. 2014.

[49] S. Golestan, J. M. Guerrero, and J. C. Vasquez, "Three-phase PLLs: A review of recent advances," *IEEE Trans. Power. Electron.*, vol. 32, no. 3, pp. 1894–1907, Mar. 2017.

[50] P. R. U. Guazzelli et al., "Decoupled predictive current control with duty-cycle optimization of a grid-tied nine-switch converter applied to an induction generator," *IEEE Trans. Power Electron.*, vol. 37, no. 3, pp. 2778–2789, Mar. 2022.

[51] W. Leonhard, *Control of Electrical Drives*, 2nd ed. Berlin, Germany: Springer, 1996.

Paulo Roberto Ubaldo Guazzelli received the B.E. degree (Hons.) in electrical engineering from the Federal University of São Carlos (UFSCar), São Paulo, Brazil, in 2014, and the M.Sc. and Ph.D. degrees from the University of São Paulo (USP), São Paulo, in 2017 and 2021, respectively.

He is a Postdoctoral Fellow with the São Carlos School of Engineering, University of São Paulo. He is currently a Professor with the Department of Electrical Engineering, Federal University of São Carlos. His research interests include electric machine drives, power electronics, and model predictive control.

Stefan Thiago Cury Alves dos Santos received the B.Eng. (Hons.) and M.Eng. degrees in electrical engineering in 2017 and 2021, respectively, from the School of Engineering of São Carlos, University of São Paulo, São Paulo, Brazil, where he is currently working toward the Ph.D. degree in electrical engineering.

His research interests include sensorless control of electric machine drives, control systems, and power electronics.

José Roberto Boffino de Almeida Monteiro (Member, IEEE) received the bachelor's degree from the School of Engineering of São Carlos, University of São Paulo (USP), São Paulo, Brazil, in 1994, and the master's and Ph.D degrees from the School of Engineering of São Carlos, USP, in 1997 and 2002, respectively, all in electrical engineering.

He is currently a Professor with the Department of Electrical Engineering, School of Engineering of Sao Carlos, USP, where he teaches power electronics and electric machines. His main research interests include electric machines, permanent magnet machines, power electronics, and control.

Manoel Luís de Aguiar received the B.Eng. degree in electrical engineering from the Federal University of Uberlândia, Uberlândia, Brazil, the master's degree in electrical engineering from the Department of Electrical Engineering, School of Engineering of São Carlos, University of São Paulo (USP), São Paulo, Brazil, and the Ph.D. degree in electrical engineering from the Institute of Electronics, Technical University of Berlin, Berlin, Germany, in 1983, 1987, and 1994, respectively.

Since 1986, he has been with the Department of Electrical Engineering, School of Engineering of São Carlos, São Paulo, Brazil, in the areas of power electronics, machines and drives, and controls systems.